JOM, Vol. 73, No. 6, 2021
https://doi.org/10.1007/s11837-021-04675-1
© 2021 The Minerals, Metals & Materials Society

Influence of Process Parameters on Mechanical and Corrosion Behavior of DED-Processed Biomedical Ti-35Nb-7Zr-5Ta Alloy

MOHAN SAI KIRAN KUMAR YADAV NARTU,[1,2] DAVID FLANNERY,[1,2] SANGRAM MAZUMDER,[1,2] SRINIVAS A. MANTRI,[1] SAMEEHAN S. JOSHI,[1] ADITYA V. AYYAGARI,[2] BRANDON MCWILLIAMS,[3] KYU CHO,[3] NARENDRA B. DAHOTRE,[1,2] and RAJARSHI BANERJEE[1,2,4]

1.—Center for Agile and Adaptive Manufacturing, University of North Texas, Denton 76207, USA. 2.—Department of Materials Science and Engineering, University of North Texas, Denton 76207, USA. 3.—Weapons and Materials Research Directorate, U.S. Army Research Laboratory, Aberdeen Proving Ground, MD 21005, USA. 4.—e-mail: Raj.banerjee@unt.edu

The laser-engineered net-shaping (LENS^{TM}) process was employed for directed energy deposition (DED) of Ti-35Nb-7Zr-5Ta (wt.%) or TNZT, a low modulus metastable β-Ti alloy for biomedical applications. The laser power was varied in the range of 400–600 W, while keeping all other parameters constant. A change in the overall grain morphology was noted in the sample with an increase in the laser power. The higher laser power samples showed more columnar grains compared to the equiaxed grains observed in the 400-W condition. The DED-processed TNZT alloys exhibited a combination of high tensile yield strength ($\sim$ 500 MPa) and ductility ($\sim$ 25%). Moreover, the alloys also exhibited excellent corrosion resistance in Ringer's solution. Overall, the results indicate that the LENS-deposited TNZT alloy could be a promising candidate for biomedical applications.

INTRODUCTION

Over the last few years, (metastable) β-Ti alloys have been widely explored for various structural applications due to their lower elastic modulus, higher specific strength, enhanced fracture toughness, and enhanced fatigue resistance compared to α or α+β Ti alloys.[1–5] Their improved corrosion resistance as well as higher hydrogen tolerance makes them perform better than the α/α+β Ti alloys in particular environments.[6–8] Ti-6Al-4V, an α+β alloy, commercially known as Ti-64, has been employed for biomedical implant applications for decades.[9] However, the presence of vanadium (V) in this alloy can lead to toxicity upon reaction with the physiological environment.[10] Furthermore, a relatively high elastic modulus of Ti-64 compared to human bone can cause stress shielding effects, adding to the challenges during orthopaedic applications.[11–14]

(Received January 26, 2021; accepted March 29, 2021; published online April 19, 2021)

In light of this, a variety of low-toxic and low-elastic modulus β-Ti alloys have been explored to promote the load sharing between the bone and the metal-based implant.[15,16] Among them, Ti-Nb-Zr-Ta alloys are quite attractive due to their lower elastic modulus ($\sim$ 55 GPa compared to $\sim$ 40 GPa of structural human bone) and excellent biocompatibility. The Ti-35Nb-7Zr-5Ta (TNZT) alloy has been well established as a biomedical alloy, and is currently being commercially used in the conventionally processed form (cast + forged) for biomedical applications as "TiOsteum®", including for stems in hip implants.[13,17] Conventionally processed TNZT alloy in its solution-treated condition exhibits a strength of 530 MPa and an elongation of 20%.[14] These authors also reported[15] an enhancement in the yield strength of TNZT to 1288 MPa, accompanied by an increase in modulus, either by increasing the oxygen content or by artificial aging. These improvements make them attractive candidates for other biomedical applications, such as screws. Chan et al.[16] in their study claimed that

laser processing on surface of the TNZT alloy led to an improvement in wear and corrosion resistance over the untreated alloy. On the other hand, preliminary in vitro studies performed on the TNZT alloy fabricated by laser-engineered net-shaping (LENS^{TM}, a powder-fed laser additive manufacturing technique) indicate substantial enhancement in bone cell differentiation of bone marrow stem cells as compared with Ti-64.[18] Furthermore, by introducing a homogenous distribution of ceramic phases like borides into the TNZT matrix via the LENS process, the wear resistance has been shown to improve.[19] DED processing techniques, such as LENS, can also be employed for processing functionally graded alloys, with varying elastic moduli, to reduce the effects of stress shielding associated with the modulus mismatch.[20] Although, AM techniques are quite promising for processing β-Ti alloys, as discussed in the previous sections, other challenges associated with AM, like optimizing the laser power parameters, growth of columnar grains, development of $<001>\beta$ texture along the build direction, porosity, and compositional control, still need to be addressed.[21–25] The principal objectives of this study are to investigate the influence of laser power on mechanical and corrosion properties of LENS-processed TNZT, and to investigate the effect of laser power on the evolution of porosity, β texture along the build direction, grain size, and morphology.

MATERIALS AND METHODS

An Optomec LENS-750 was used for fabricating TNZT alloys on a Ti-64 seed plate. Pre-alloyed TNZT powder obtained from Tosoh SMD was used during DED. A 1500-W Nd: YAG laser that produces near-infrared radiation at a wavelength of 1.064 μm was used for the deposition. Three different laser powers, 400 W, 500 W, and 600 W, were used for fabricating TNZT. All the other processing parameters were kept constant and were 0.5 mm laser beam size and 12.7 mm/s laser linear scanning rate. These combinations of laser parameters provided input energy densities of 51.95×10^3 J/mm^2, 64.94×10^3 J/mm^2 and 77.92 J/mm^2 for the fabrication of TNZT. Each layer was fabricated by laying down consecutive multiple linear laser track deposits. The laser track (hatch) deposit width was maintained at 0.381 mm and the laser track (hatch) deposit spacing (center to center distance between two consecutive tracks) was 0.254 mm. A cube of dimensions of $25.4 \times 25.4 \times 25.4$ mm was fabricated for each condition. The oxygen level in the build chamber was kept below 10 ppm during all the DED experiments with the aid of a 99.99% pure Ar atmosphere.

The deposited builds were then separated from the seed plate and subsequently sliced into two sections along the build direction using a KENT USA (WSI-200) electrical discharge machine. One of the two sections were finely polished to 0.02 μm for microstructural analysis and the other section was utilized for machining tensile specimens with gauge length $\sim$ 5mm, width $\sim$ 1 mm, and thickness $\sim$ 0.7–1 mm. The tensile specimens were machined perpendicular to the build direction and the tests were performed at a strain rate of 10^{-3} s^{-1}. At least three tensile specimens were tested for each condition, and the plots with median values of tensile strength and ductility were reported.

X-ray diffraction (XRD) studies were performed on the polished samples (along the cross-section) using a Cu-Kα Rigaku Ultima III diffractometer. The microstructure was characterized using a FEI Nova NanoSEM 230, equipped with electron backscattered diffraction (EBSD) and energy dispersive spectroscopy detector. OIM^{TM} software was used for generating texture plots from the EBSD data.

Anodic polarization tests were carried out on all the three conditions of the LENS-deposited TNZT samples. Specimens of 15 mm diameter were machined from the TNZT deposits and polished to an average surface finish of 0.2 μm for this purpose. The samples were then cleaned ultrasonically and employed as the working electrode in the test cell. The tests were carried out in a simulated body solution known as Ringer's solution, which has a composition of NaCl 9 g/L, KCl 0.43 g/L, $CaCl_2$ 0.24 g/L, and $NaHCO_3$ 0.2 g/L. Open circuit potential (OCP) of the alloys was then monitored. The room-temperature anodic polarization tests were performed from an initial potential of $-$ 0.5–9 V with respect to the OCP. A scan rate of 0.166 mV/s and the current density was recorded continuously. A saturated calomel electrode was used as a reference electrode and a platinum wire as a counter electrode.[26] The tests were repeated to ensure the reproducibility of the data obtained.

RESULTS AND DISCUSSION

Analysis of Pre-alloyed TNZT Powders

Figure 1a shows the gas-atomized TNZT powders. As can be seen, the powders are spherical in shape which leads to good flowability, a very important factor for DED processing. The powder size distribution in Fig. 1b, obtained using a Microtrac SPC3500 powder particle analyzer, shows d_{90} to be in the range of 65 $\pm$ 55 μm, which is close to the ideal size range for DED processing. The powder particles seem to have a dendrite-like structure, based on scanning electron microscope (SEM) observations. The XRD pattern obtained from the powder shows single-phase bcc β-Ti peaks, confirming previous reports in the literature.[27,28]

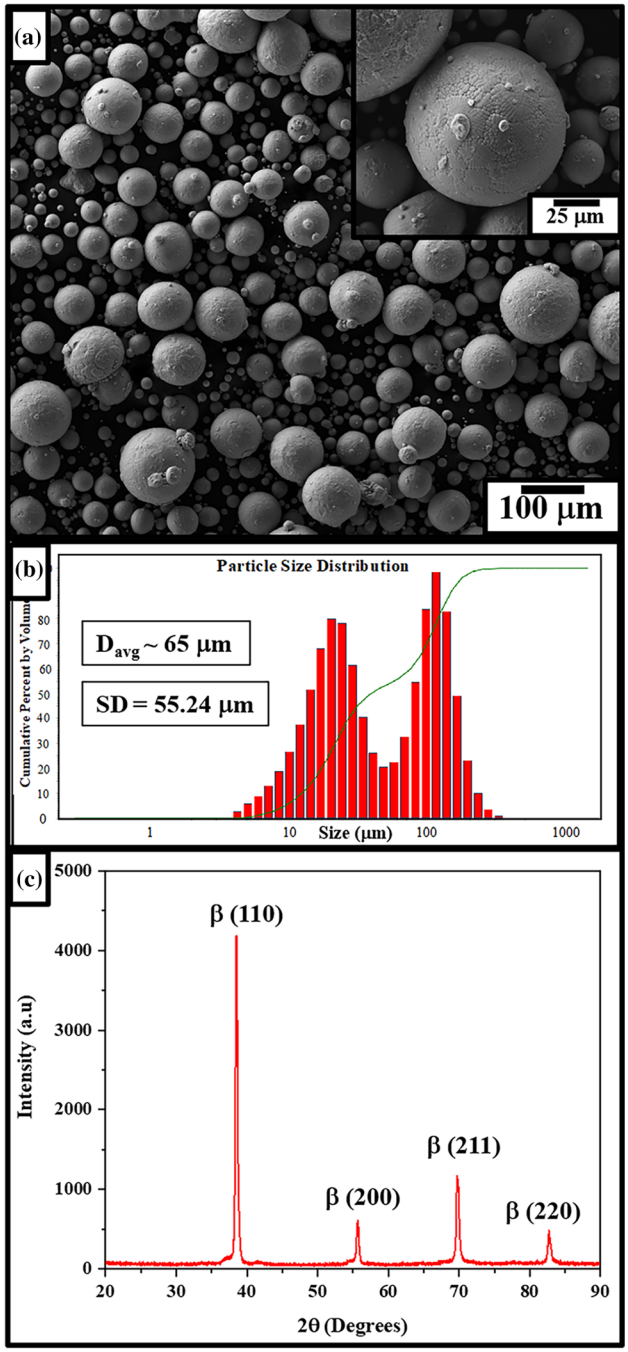

Fig. 1. (a) SEM of pre-alloyed TNZT powder with inset showing the higher magnification image, (b) particle size distribution, (c) XRD of TNZT powder showing single phase β-bcc peaks.

MICROSTRUCTURE AND PHASE ANALYSIS

Following the deposition, as mentioned before, the samples were sectioned into two halves. The XRD analysis and SEM micrographs of all the three conditions, i.e., 400 W, 500 W, and 600 W, are shown in Fig 2. While the sample which was processed under 400 W showed only β-peaks in the XRD studies, the 500-W and 600-W samples also showed the presence of α peaks. This is probably due to the higher energy densities obtained by using the higher processing wattages.[9,22] Similar observations were also noted in the SEM images of the three different conditions. The images shown in Fig. 2b, c, and d represent the low, medium, and high magnification SEM backscattered images, respectively, obtained from the 400-W condition. Fig. 2e–g and h–j represent the same obtained from 500-W and 600-W conditions, respectively. The microstructure in all three cases consist of coarse β grains. The low magnification SEM images (Fig. 2b and h) obtained from the 400-W and 600-W conditions reveal the presence of two types of porosities, process-induced porosity (PIP) and gas-induced porosity (GIP), based on the dimensions and the morphology of the pores.[9,22] Typically, the pores formed due to the processing PIP are non-spherical in nature, and their size can range from sub-microns to macroscopic, in contrast to the micron-level GIP which are spherical, as shown in Fig. 2b and h, respectively. The inert gas (Ar) employed in the LENS system is insoluble in liquid metals and

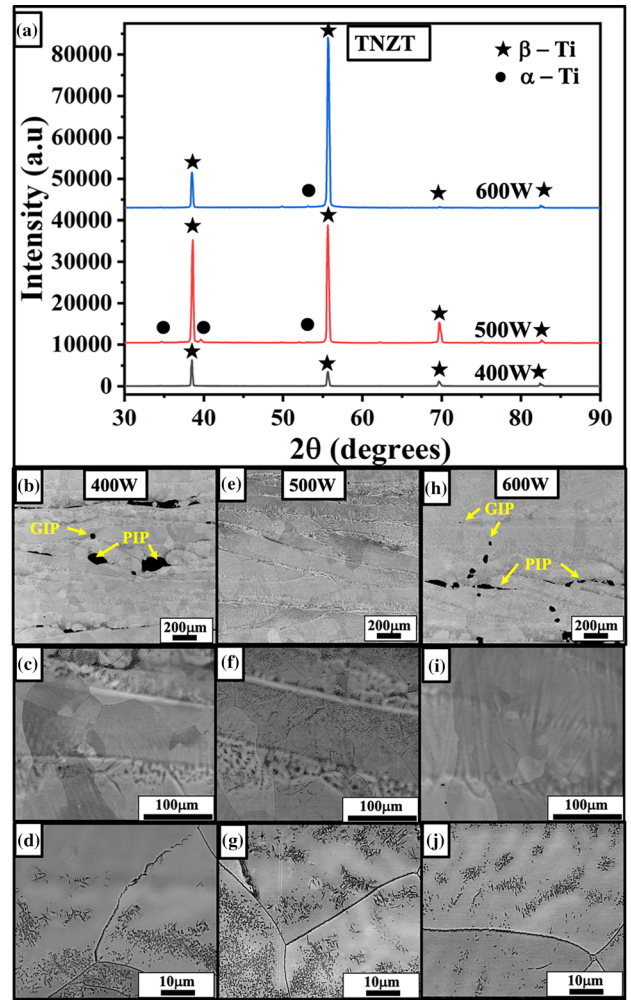

Fig. 2. (a) XRD plot identifying β and α phases present in the three conditions of LENS^{TM} manufactured TNZT alloy. SEM backscattered images showing the microstructures of (b–d) 400 W, (e–g) 500W and (h–j) 600 W conditions of the same alloy.

therefore can be easily trapped creating intralayer porosity in the solidified pool. The remelting of the previously deposited layers during the laser processing has been shown to release the trapped gas, reducing the porosity.[29,30] Therefore, with the increase in laser power from 400 W to 500 W, the effect of remelting/reheating of the previously deposited layers increases, leading to an overall reduction in intralayer porosity. However, a further increase in laser power to 600 W might have led to the formation of the interlayer porosity. Kumar et Al. have shown that the viscosity of the molten metal increases with the increase in energy density, resulting in poor spreading of the liquid metal over the previously deposited layers, leading to interlayer porosity or a lack of fusion porosity.[29,31] No signs of micro-segregation of any beta-stabilizing elements is observed in the backscattered SEM images. However, faint cellular like sub-grain structures can be clearly observed in all the conditions. Furthermore, the high magnification SEM images (Fig. 2d, g, and j) reveal the presence of fine-scale α precipitates in all the cases.

It is also important to understand the nature of the grain growth in these DED-processed samples, as they affect the mechanical behavior by leading to anisotropy,[22–25] and, as such, the EBSD analysis was carried out on all the three conditions along the build direction. Figure 3 shows the inverse pole figure (IPF) maps with corresponding texture plots (on the right) from top, middle, and bottom regions (along the build direction) of the 400-W, 500-W, and 600-W conditions. The microstructures corresponding to the 400-W condition (Fig. 3a–c) appear to consist primarily of equiaxed grains along the build direction. An average grain size of $\sim$ 40 μm was noted in the bottom region and it increased to $\sim$ 60 μm in the middle regions. The grain size further increased to about $\sim$ 100 μm in the top-most region. This trend seemed to continue for the samples processed at 500 W and 600 W. While the microstructures from the 500-W, and 600-W conditions (Fig. 3d–i) appear to have more columnar grains, there was also an overall increase compared to the 400-W sample. This is to be expected, as an increase in the overall wattage leads to an overall increase in the energy density. Some micro-texturing along the $<001>\beta$ build direction is also observed for all three conditions. EBSD was also performed on the top surface of the build and is presented in Fig. 4. A slight increase in the micro-texture and a noticeable increase in the grain size is observed with an increase in laser power for the top surface. This is also noted in the XRD analysis, in which an increase in the laser wattage showed an increase in the $<001>\beta$ texture.

Another important aspect of this study was to better understand the composition–processing–microstructure relationships of the as-deposited alloys. The composition of the alloy, along with the processing conditions, plays an important role in the final microstructure. In our previous studies on another β-Ti alloy,[21] Ti-20V exhibited columnar grains, in the range of 2–3 mm, along the build

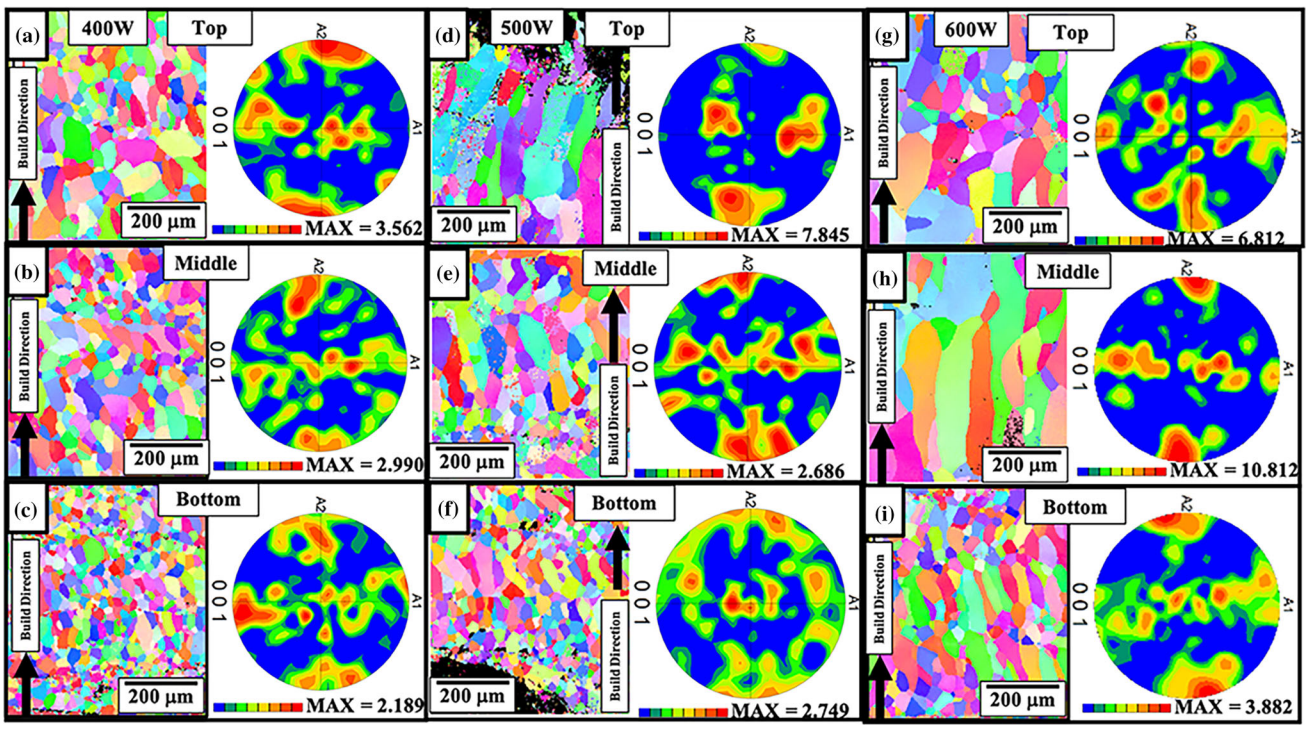

Fig. 3. Inverse pole figure (IPF) maps with corresponding texture plots (on the right) obtained from top, middle and bottom regions along the build direction of (a–c) 400 W, (d–f) 500 W and (g–i) 600 W conditions of LENS^{TM} manufactured TNZT alloy.

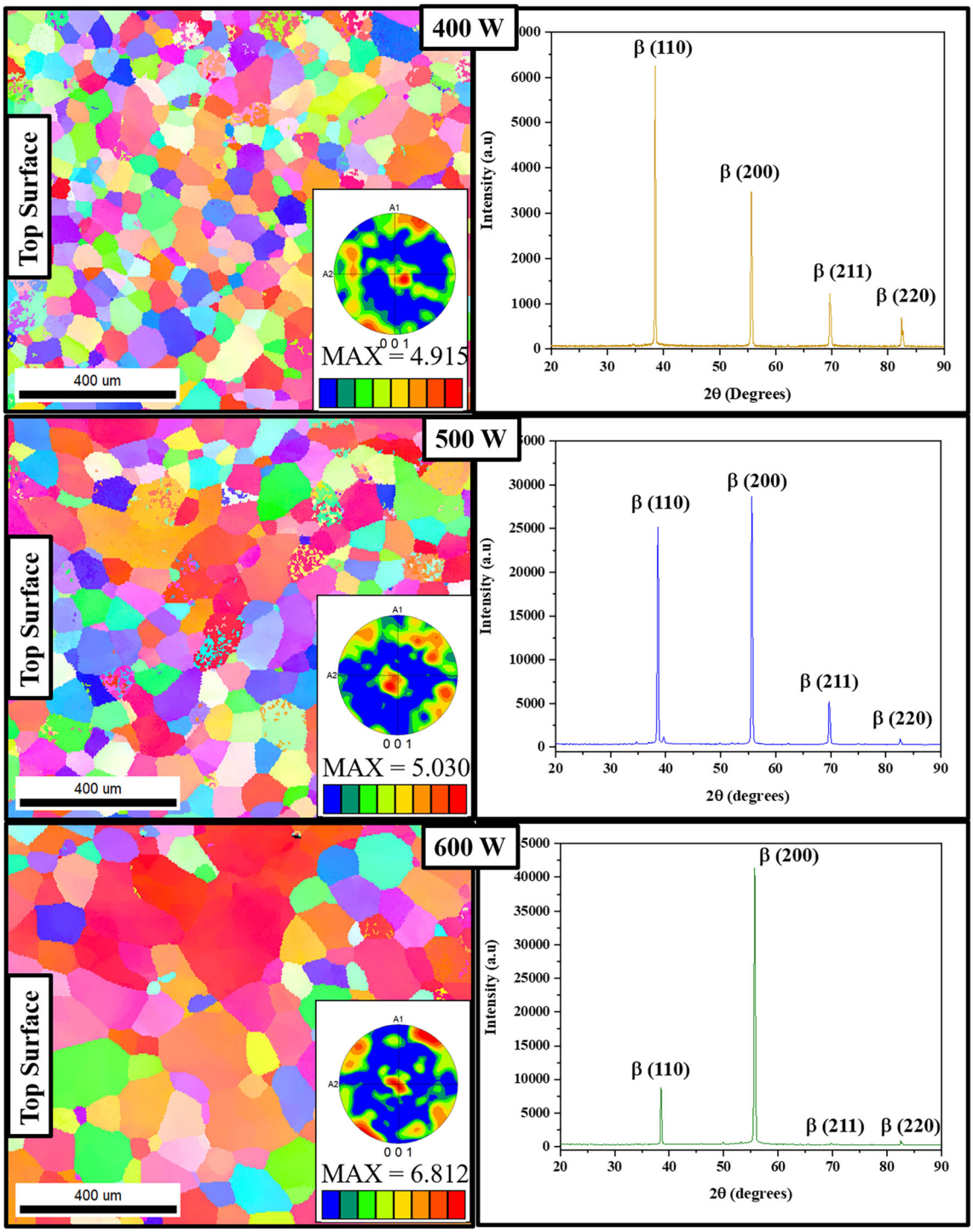

Fig. 4. Inverse pole figure (IPF) maps with corresponding texture plots and XRD plots obtained perpendicular to the build direction of 400 W, 500 W, 600 W conditions of LENS manufactured TNZT alloy.

direction. Even though all the processing conditions were kept the same, there is an incremental change in the overall grain size of the binary Ti-20V alloy, compared to the present TNZT. An EBSD IPF map and corresponding texture plot are shown in Fig 5. In an attempt to understand this difference between the two alloys, the solidification curves for the TNZT and Ti-20V systems have been simulated, based on Scheil equations, using the solution thermodynamics-based PANDAT™ software.[32]

The solidification curves for the TNZT and Ti-20V alloys are shown in Fig. 5a and b, respectively. The calculated solidification range for TNZT is ~ 220°C, which is significantly more than the value

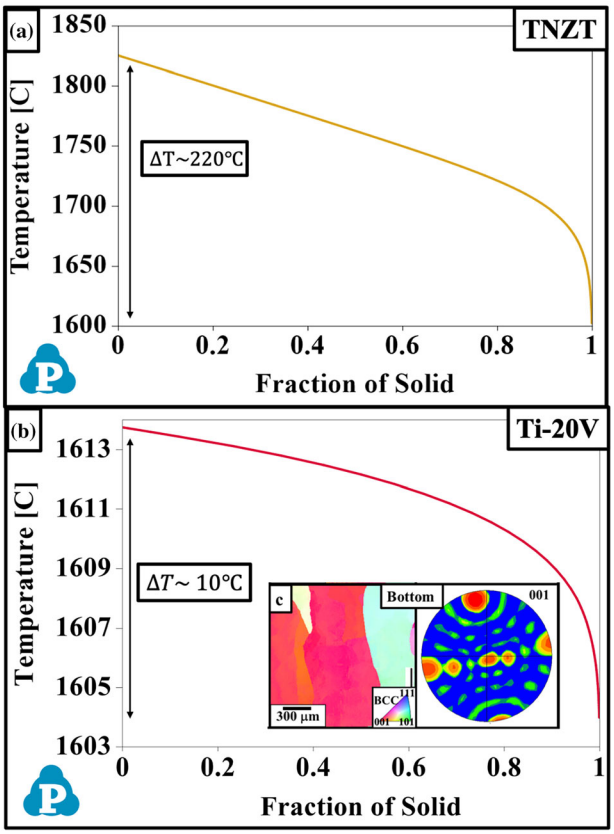

Fig. 5. Solidification curves for (a) TNZT and (b) Ti-20V alloys simulated based on Scheil equations using PANDAT™ software. (c) Inset shows IPF and texture plot of Ti-20V sample.

calculated for Ti-20V (~ 10°C). Based on the fundamentals of solidification in metal/alloy systems, a critical level of undercooling (ΔT_c) is required for the formation of a stable, spherical, solid nucleus inside the liquid metal/alloy. The solidification process can only take place when certain regions within the liquid overcome the critical free energy barrier (ΔG^*). This nucleation barrier, based on homogenous nucleation theory, can be described as follows[33]:

$$\Delta G^* = \frac{\left[16\pi(\gamma_{SL})^3(T_m)^2\right]}{3(\Delta T_c)^2(\Delta H_m)^2}$$

$$N \sim A \times exp\left(\frac{-\Delta G^*}{KT}\right)$$

where ΔG* is the critical nucleation barrier; γSL is the liquid solid interfacial free energy per unit area; Tmis is the melting temperature; ΔTc is the critical undercooling; ΔHm is the latent heat of fusion; N is the nucleation rate, A is a constant based on diffusivity, K is the Boltzman constant, and T is the temperature of the liquid metal/alloy

Based on the above expressions, it can be realized that increasing the level of undercooling (ΔT_c) decreases the critical nucleation barrier (ΔG^*),

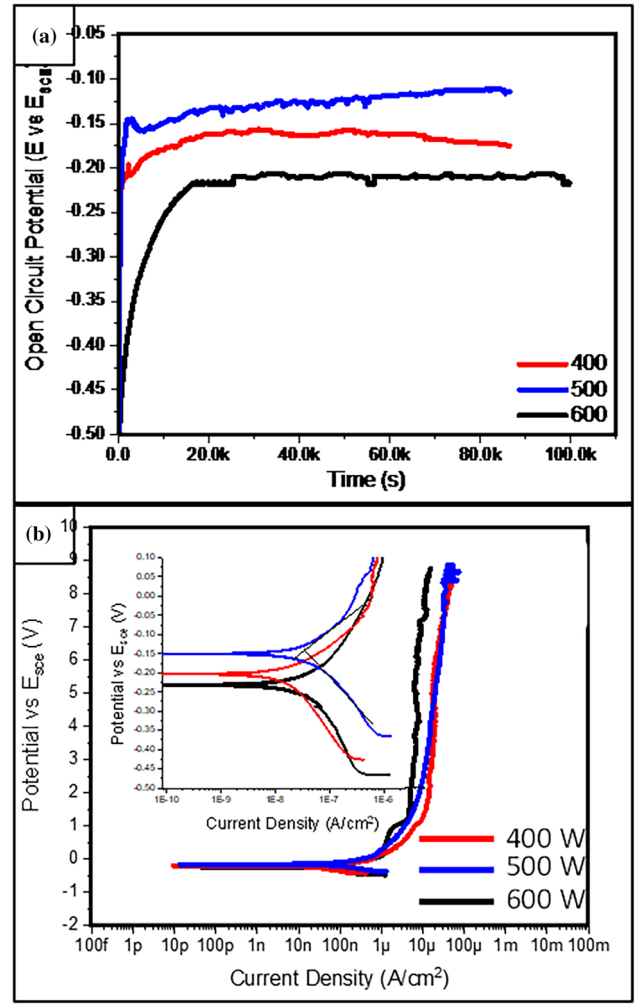

Fig. 6. (a) Open Circuit Potential & (b) Anodic Polarization curves for the three conditions of LENS™ manufactured TNZT alloy that were tested in simulated body fluid (SBF) solution.

which in turn increases the rate of nucleation (N). A higher nucleation rate results in a higher number density of simultaneously growing nuclei, suppressing the extent of grain growth (growth of the stable nuclei) due to hard impingement with the neighboring grains, resulting in a finer equiaxed microstructure. The large solidification range in TNZT (Fig. 5a) allows the alloy melt to attain higher levels of undercoolings prior to the onset of nucleation and therefore increases the tendency to form an equiaxed microstructure, as compared to Ti-20V (Fig. 5b).

CORROSION STUDIES AND MECHANICAL TESTING

To investigate the corrosion behavior of these DED-fabricated TNZT alloys, anodic polarization tests were conducted in a simulated body fluid (SBF) solution known as Ringer's solution. Prior to performing the tests, the OCP were monitored for all three conditions (Fig. 6a). The OCP in all the

cases appeared to stabilize within a short time for all the samples. However, the sample processed with 500 W appeared to have highest stabilized OCP followed by 400 W and 600 W, respectively. Notably, the difference in OCP of 500-W and 400-samples was small (0.025–0.05 V), whereas the OCP of the 600-W sample was lower by 0.1 V compared to the 500-W sample. The higher value of OCP is considered to be better for corrosion resistance. In addition, a stable OCP as a function of time indicates an adherent and fully covered passive film. In view of this, although the 500-W sample had the highest value of OCP, the OCP experienced frequent ups and downs, suggesting the breaking and re-passivation of the film in this case. The 600-W sample had similar drops and rises in the OCP. However, the sample processed with 400-W laser power showed the best combination of OCP values and a stable nature of the OCP curve as a function of time (Fig 6a).

The corrosion potential and the corrosion current for the LENS TNZT alloys were measured using potentiodynamic polarization. The corrosion potential decreased with an increase in laser power from 400 to 500 W (Fig. 6a; Table I). However, the corrosion potential increased again with a further increase in the laser power to 600 W. On the other hand, the corrosion current steadily increased with an increase in the laser power (Fig. 6b; Table I). The higher corrosion potential for 400 W can be related to the predominant presence of GIP and PIP during the fabrication process (Fig. 2b–d). However, the α phase was lowest in the case of 400 W, leading to a lower corrosion current due to reduced galvanic coupling (Fig. 2b–d). With an increase in the laser power, although the porosity reduced, an α phase was formed in the increasing amount (Fig. 2e–g). This would have resulted in a lowering of the corrosion potential, but an increase in the corrosion current, due to micro-galvanic activity. For the highest laser power condition corresponding to 600 W, the microstructure consisted of a higher fraction of PIP and the α phase compared to the 400-W condition. Such a microstructure resulted in the highest corrosion current and a highest corrosion potential. It has been reported in the case of β Ti alloys that localized microstructural features, such as porosity and α precipitates, can lead to a material exhibiting the lower corrosion potential but a higher corrosion current.[34,35] Furthermore, for Ti alloys, it has been observed that the corrosion potential decreases with a reduction in pore content.[36] Elongated pores such as PIP have a deleterious effect on the corrosion compared to the spherical pores.[36] The corrosion potential reflects the thermodynamic possibility for the process of corrosion to occur, whereas the corrosion current reflects the kinetics/rate aspects of the corrosion reaction.

Another important observation was regarding the active to passive transition, which corresponds to the formation of a passive protective oxide film on the surface of the alloy. The integrity of the passive oxide film formed is critical for biomedical implants. In the case of stainless steels and Co-Cr-Mo alloys, the passive oxide film formed breaks down at approximately 300–500 mV (E_{bp}, breakdown potential), which can easily be attained in the body during an inflammation.[37] In the present study, none of the three conditions of LENS-deposited TNZT exhibited any breakdown of the protective oxide film formed on the surface, even at potentials as high as 9 V. The substantially higher values of E_{bp} (> 9V) indicate that all the three conditions of the LENS-processed TNZT have superior corrosion resistance in SBF. Based on these observations, the best combination of corrosion properties was obtained for the 500-W condition, which possessed the lowest corrosion potential among all the conditions and a relatively low corrosion current. Moreover, this condition also had the lowest amount of porosity which is expected to show a better set of mechanical properties. In light of this, the mechanical behavior of the 500-W TNZT sample was evaluated using tensile tests.

The engineering stress–strain curves for the bottom, middle, and top sections of the 500-W condition are shown in Fig 7. This was carried out in order to check if there would be any discrepancies based on the location of the build, and also due to the observed changes in the microstructure (Fig. 2). The bottom section exhibits a yield strength of ~ 520 MPa, while the middle and top sections show slightly lower values (~ 480 MPa). On the other hand, the highest ductility of ~ 30% is observed in top section, followed by the middle (~ 27%) and the bottom (~ 17.5%) sections. The values for the yield strength and ductility are listed in Table S1. The bottom section, which has the highest amount of α precipitation, has the highest strength and lowest ductility.[21] Moreover, the yield strength values obtained for the LENS-processed TNZT alloys in

Table I. Open circuit potential and corrosion current density values for all the conditions of LENS-manufactured TNZT alloy

Laser power (W)	Corrosion potential (mV)	Corrosion current (nA/cm^2)
400	− 200	25.61
500	− 140	38.61
600	− 225	51.12

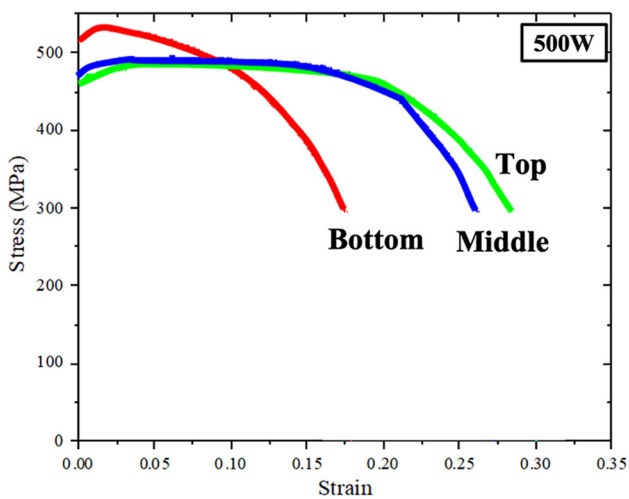

Fig. 7. Engineering stress-strain curves for the bottom, middle and top sections of the 500W condition of the same alloy.

the present study are in excellent agreement with the values reported for the conventionally processed TNZT, which is ~ 530 MPa.[13,17]

CONCLUSIONS

A biomedical β-Ti alloy, Ti-35Nb-7Zr-5Ta, was processed using the directed energy deposition technique of laser-engineered net-shaping. A change in the energy density brought about by a change in the laser power led to a change in the overall grain morphology and microtexture. Going from 400 W to 500 W and subsequently 600 W resulted in an increase in the grain size from 40 μm to 100 μm. Precipitation of secondary phases (mainly a) was noted in the samples which used higher laser powers. The 500-W sample, which had the least amount of porosity, showed good corrosion resistance in Ringer's solution. A good combination of corrosion resistance, high strength, and phenomenal ductility makes the DED-processed TNZT alloy an ideal candidate for load-bearing biomedical applications.

ACKNOWLEDGEMENTS

The authors acknowledge part financial support for this work from two different cooperative agreements between the U.S. Army Research Laboratory (ARL) and the University of North Texas; W911NF-19-2-0011 and W911NF-16-2-018.

CONFLICT OF INTEREST

The authors declare that they have no conflict of interest.

SUPPLEMENTARY INFORMATION

The online version contains supplementary material available at https://doi.org/10.1007/s11837-021-04675-1.

REFERENCES

1. R.P. Kolli and A. Devaraj, *Metals (Basel)* 8, 1 (2018).
2. P. Laheurte, F. Prima, A. Eberhardt, T. Gloriant, M. Wary, and E. Patoor, *J. Mech. Behav. Biomed. Mater.* 3, 565 (2010).
3. D. Kuroda, M. Niinomi, M. Morinaga, Y. Kato, and T. Yashiro, *Mater. Sci. Eng. A* 243, 244 (1998).
4. O.M. Ivasishin, P.E. Markovsky, Y.V. Matviychuk, S.L. Semiatin, C.H. Ward, and S. Fox, *J. Alloys Compd.* 457, 296 (2008).
5. F.H. Froes, *Titanium: physical metallurgy, processing, and applications* (ASM International, Materials Park, 2015).
6. G. Lütjering and J.C. Williams, *Titanium* (Springer, Cham, 2007).
7. R.R. Boyer and R.D. Briggs, *J. Mater. Eng. Perform.* 22, 2916 (2013).
8. I. Weiss, and S.L. Semiatin, *Mater. Sci. Eng. A* 243, 46 (1998).
9. W.E. Frazier, *J. Mater. Eng. Perform.* 23, 1917 (2014).
10. M. Niinomi and C.J. Boehlert, *Titanium alloys for biomedical applications* (Springer, Berlin, 2015), pp 179–213.
11. J.L. Domingo, *Biol. Trace Elem. Res.* 88, 97 (2002).
12. M.T. Mohammed, Z.A. Khan, and A.N. Siddiquee, *Int. J. Chem. Mol. Nucl. Mater. Met. Eng.* 8, 726 (2014).
13. M. Geetha, A.K. Singh, R. Asokamani, and A.K. Gogia, *Prog. Mater. Sci.* 54, 397 (2009).
14. J. Qazi, V. Tsakiris, B. Marquardt, and H. Rack, *J. ASTM Int.* **2** (8), 1 (2005). https://doi.org/10.1520/JAI12780.
15. J.I. Qazi, H.J. Rack, and B. Marquardt, *JOM* 56, 49 (2004).
16. C.-W. Chan, S. Lee, G. Smith, G. Sarri, C.-H. Ng, A. Sharba, and H.C. Man, *Appl. Surf. Sci.* **367**, 80–90 (2016). https://doi.org/10.1016/j.apsusc.2016.01.091.
17. H.J. Rack and J.I. Qazi, *Mater. Sci. Eng. C* 26(8), 1269 (2006).
18. S. Samuel, S. Nag, S. Nasrazadani, V. Ukirde, M. El Bouanani, A. Mohandas, K. Nguyen, and R. Banerjee, *J. Biomed. Mater. Res. Part A* 94A, 1251 (2010).
19. S. Samuel, S. Nag, T.W. Scharf, and R. Banerjee, *Mater. Sci. Eng. C* 28, 414 (2008).
20. D.D. Lima, S.A. Mantri, C.V. Mikler, R. Contieri, C.J. Yannetta, K.N. Campo, E.S. Lopes, M.J. Styles, T. Borkar, R. Caram, and R. Banerjee, *Mater. Des.* 130, 8 (2017).
21. S.A. Mantri and R. Banerjee, *Addit. Manuf.* 23, 86 (2018).
22. W.J. Sames, F.A. List, S. Pannala, R.R. Dehoff, and S.S. Babu, *Int. Mater. Rev.* 61, 315 (2016).
23. M. Simonelli, Y.Y. Tse, and C. Tuck, *Metall. Mater. Trans. A* 45, 2863 (2014).
24. T.M. Butler, C.A. Brice, W.A. Tayon, S.L. Semiatin, and A.L. Pilchak, *Metall. Mater. Trans. A* 48, 4441 (2017).
25. N. Sridharan, A. Chaudhary, P. Nandwana, and S.S. Babu, *JOM* 68, 772 (2016).
26. A.V. Aditya, H.S. Arora, and S. Mukherjee, *J. Non-Cryst. Solut.* 425, 124 (2015).
27. R. Ummethala, P.S. Karamched, S. Rathinavelu, N. Singh, A. Aggarwal, K. Sun, E. Ivanov, L. Kollo, I. Okulov, J. Eckert, and K.G. Prashanth, *Materials* 14, 100941 (2020).
28. E. Ivanov, E. del Rio, I. Kapchemnko, M. Nyström, and J. Kotila, *Key Eng. Mater.* 770, 9 (2018).
29. Z. Yu, Y. Zheng, J. Chen, C. Wu, J. Xu, H. Lu, and C. Yu, *J. Mater. Process. Technol.* 284, 116738 (2020).
30. T. DebRoy, H.L. Wei, J.S. Zuback, T. Mukherjee, J.W. Elmer, J.O. Milewski, A.M. Beese, A. Wilson-Heid, A. De, and W. Zhang, *Prog. Mater. Sci.* 92, 112 (2018).
31. G. Kumar and K. Prabhu, *Adv. Colloid Interface Sci.* 133(2), 61 (2007).

32. S.-L. Chen, S. Daniel, F. Zhang, Y.A. Chang, X.-Y. Yan, F.-Y. Xie, R. Schmid-Fetzer, and W.A. Oates, *Calphad* 26, 175 (2002).
33. D.A. Porter, K.E. Easterling, and M. Sherif, *Phase Transformations in Metals and Alloys* (CRC, Boca Raton, 2009).
34. I. Cvijović-Alagić, Z. Cvijović, J. Bajat, and M. Rakin, *Corr. Sci.* 83, 245 (2014).
35. J. Fojt, L. Joska, and J. Málek, *Corr. Sci* 71, 78 (2013).
36. K.H.W. Seah, R. Thampuran, and S.H. Teoh, *Corr. Sci.* 40, 547 (1998).
37. H. Zitter and H. Plenk Jr., *J. Biomed. Mater. Res.* 21, 881 (1987).

Publisher's Note Springer Nature remains neutral with regard to jurisdictional claims in published maps and institutional affiliations.